Nanoscale

Accepted Manuscript

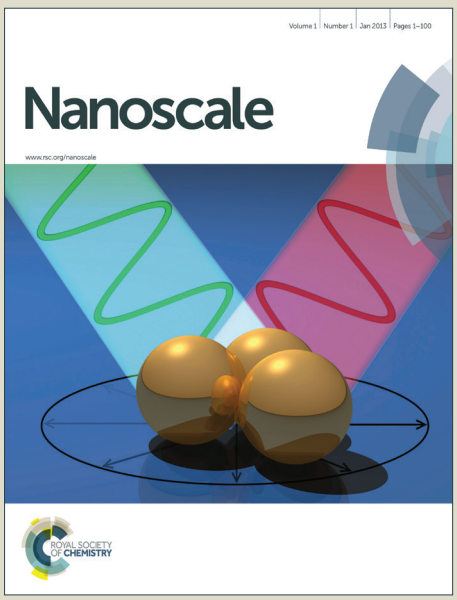

ROYAL SOCIETY OF CHEMISTRY

www.rsc.org/nanoscale

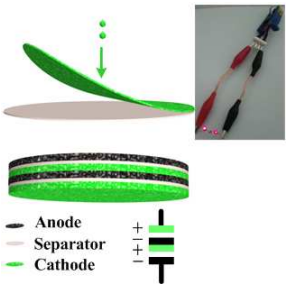

A series-wound asymmetric supercapacitor with inner-connection structure has a high output voltage of 4.0 V and can derive two LEDs connected in series.

Series Asymmetric Supercapacitors Based on Free-standing Inner-Connection Electrodes for High Energy Density and High Output Voltage

Jiayou Tao,[a] Nishuang Liu,[a] Jiangyu Rao,[a] Longwei Ding,[a] Majid Raissan AL Bahrani,[a] Luying Li,[a] Jun Su[a] & Yihua Gao*[a,b]*

[a] Center for Nanoscale Characterization & Devices (CNCD), Wuhan National Laboratory for Optoelectronics (WNLO)-School of Physics, Huazhong University of Science and Technology (HUST), LuoyuRoad 1037, Wuhan 430074, P. R. China

[b]Hubei Collaborative Innovation Center for Advanced Organic Chemical Materials, 368 Youyi Avenue, Wuhan 430062, P. R. China

Correspondence and requests for materials should be addressed to Y.H.G. (gaoyihua@hust.edu.cn) & N.S.L. (nishuang_liu@foxmail.com)

Abstract: Asymmetric supercapacitors (ASCs) based on free-standing membranes with high energy density and high output voltage are reported. MnO_2 nanowires/carbon nanotubes (CNTs) composites and MoO_3 nanobelts/CNTs composites are selected as the anode and the cathode materials of the devices, respectively. The ASC has a high volumetric capacitance of 50.2 F cm^{-3} at a scan rate of 2 mV s^{-1} and a high operation voltage window of 2.0 V. Especially, after a middle layer with inner-connection structure was inserted between the anode and the cathode, the output voltage of the whole device can achieve 4.0 V. The full cell of series ASCs (SASC) with an inner-connection middle layer has a high energy density of 28.6 mWh cm^{-3} at a power density of 261.4 mW cm^{-3}, and exhibits excellent cycling performance of 99.6% capacitance retention over 10000 cycles. This strategy designing the hybridized structure for SASCs provides a promising route for next-generation SCs with high energy density and high output voltage.

1 Introduction

Electrochemical capacitors, also known as supercapacitors (SCs), are promising energy devices that bridge the gap between batteries and conventional capacitors.[1] Due to a number of features such as high power density, fast rates of charge-discharge, long cycling life and improved safe operation,[2-4] SCs have been widely used in numerous areas such as memory backup systems, hybrid electric vehicles, mobile electronic devices.[5-7] However, the relatively low energy density and output voltage have restricted their potential application. Therefore, improving operation voltage and energy density is crucial for SCs to meet the future demands in practice. Commonly, maximizing the specific capacitance and the operation potential window can significantly increase the energy density. As for high specific capacitance, intense interests focus on electrode materials with high specific surface area and high theoretical specific capacitance, such as CoO/polypyrrole manowires,[8] MnO_2/rGO nanocomposite,[9] rGO/V_2O_5 nanoparticles,[10] and so on. These distinctive nanostructures improved the chemical performance of the devices significantly. To widen the operation voltage, traditionally, there are two kinds of solutions. One is to use more suitable electrolyte that can endure higher working voltage, such as organic electrolyte and quasi solid-state electrolyte.[11, 12] The other way is to design asymmetric electrodes for SCs. ASCs can exhibit two different potential windows of the electrodes in the same electrolyte.[13-15] As a result, the potential window is widened and the energy density of the ASC could be improved. In recent years, great progress have been made in design of ASCs, such as organic-inorganic composite

electrodes,[16] metal oxide/metal hydroxide electrodes.[17] As a consequence, these devices exhibit higher operation voltages in the range of 1.0 ~ 2.0 V.

As electrode materials for SCs, transition metal oxides have higher theoretical specific capacitance and better cycling stability compared to carbon materials and conducting polymers, respectively.[18] However, pure transition metal oxides always provide low power density since they are hindered by their poor electrical conductivity.[19] CNT, a kind of one dimensional carbon material, has attracted worldwide interest by virtue of its high conductivity, high specific area, superior mechanical property. Also, CNT is a good candidate for electrode materials in energy storage,[20] but the low specific capacitance restricts its direct application as electrodes for high energy SCs.[21] Commonly, CNTs often integrate with other materials as electrodes and provide channels for electrons transferring in the electrodes. Previously, Jin and co-workers described ASCs with reduced graphene/MnO_2/CNT composite paper as a positive electrode and CNT/polyaniline (PANI) composite paper as a negative electrode in a gel electrolyte.[22] Although the device exhibited an high energy density of 24.8 Wh kg^{-1}, the relatively narrow operating window of 1.6 V and unsatisfied stability (~ 7% decay after 800 cycles) hindered its further application. Xu and co-workers have developed ASCs with Co_9S_8 nano-arrays on carbon cloth as the positive electrode and Co_3O_4/RuO_2 nanosheet arrays on carbon cloth as the negative electrode.[23] An energy density of 1.21 mWh cm^{-3} at the power density of 13.29 W cm^{-3} with a voltage window of 1.6 V in 3 M KOH aqueous solution has been achieved. The device exhibited excellent stability of 99.0% capacitance retention after 2000 cycles.

However, the elaborate procedures of fabricating and the high cost of RuO_2 lowered the industrial applicability of the device. Thus, there are still huge challenges for designing and optimizing ASCs with both high fabrication-efficiency and excellent electrochemical performance.

Here, we report the design of ASCs and SASCs based on free-standing membrane electrodes to meet the demands in practice. Our strategy is to increase potential window possibly, while maintaining high capacitance of the device. Different metal oxides and CNT composites were designed for the positive and negative electrodes, which fully exploited their high theoretical capacitance and high conductivity. To enlarge operating potential window of the devices, we have synthesized MnO_2 nanowires and MoO_3 nanobelts as the metal oxides for positive and negative electrodes. These two metal oxides have the largest work function drop (4.4 eV of MnO_2 and 6.9 eV of MoO_3, respectively)[24] that results the widest potential window of the devices. Considering that the energy density is proportional to the capacitance and to the square of the operation voltage, most commercial SCs choose organic electrolytes because of the higher operating voltages, which provide a higher energy density.[4] $LiPF_6$/organic solvent is a kind of widely used electrolyte in energy storage devices,[25, 26] which can operate steadily at a higher operate voltage in excess of 4.0 V.[26] Thus, an organic electrolyte of $LiPF_6$/Ethylene carbonate (EC)/Dimethyl carbonate (DMC) is used in our devices trying to achieve high performance. Benefiting from the rational design of the electrode active materials and the electrolyte, the as-fabricated ASC exhibits a large operating voltage window of 0 ~

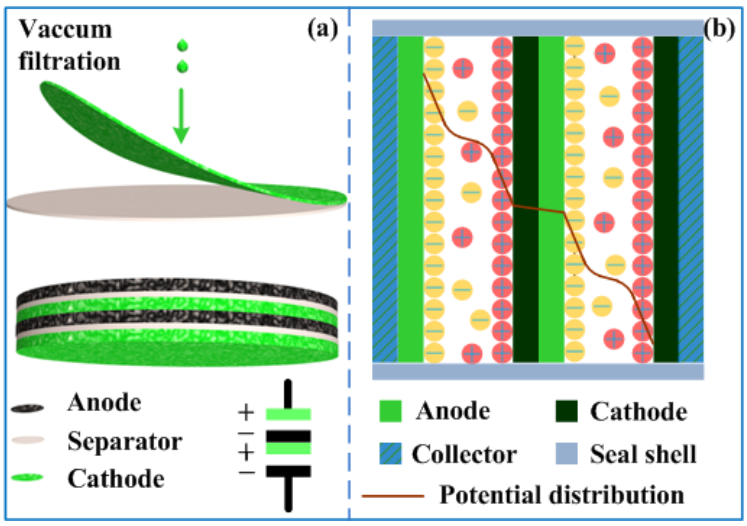

Scheme 1. Schematic of: (a) the fabrication process and hybrid structure of the SASC based on free-standing films; (b) the structure of the SASC full cell and the potential distribution in it.

2.0 V and a high volumetric capacitance of 50.2 F cm^{-3} at a scan rate of 2 mV s^{-1} in $LiPF_6$/EC/DMC electrolyte, respectively, which is much higher than the previous reports.[23] Furthermore, we designed the SASC with a hybrid structure that a middle layer was inserted between the positive (MnO_2/CNTs) and negative (MoO_3/CNTs) electrodes. The as-fabricated SASC has a voltage window of 0 ~ 4.0 V, high energy density of 28.6 mWh cm^{-3} at a power density of 261.4 mW cm^{-3}, and good long-term stability of less than 1% capacitance decay after 10000 cycles.

2 Results and Discussion

2.1 Characterizations of Positive Electrode Materials

The fabrication process of ASC and SASC is described in Scheme 1(more details of the experiment are showed in Supporting Information). Free-standing membranes are prepared by simple vacuum filtration technique. When the films were dried completely, they were cut to suitable area, then sealed in a coin cell with an organic

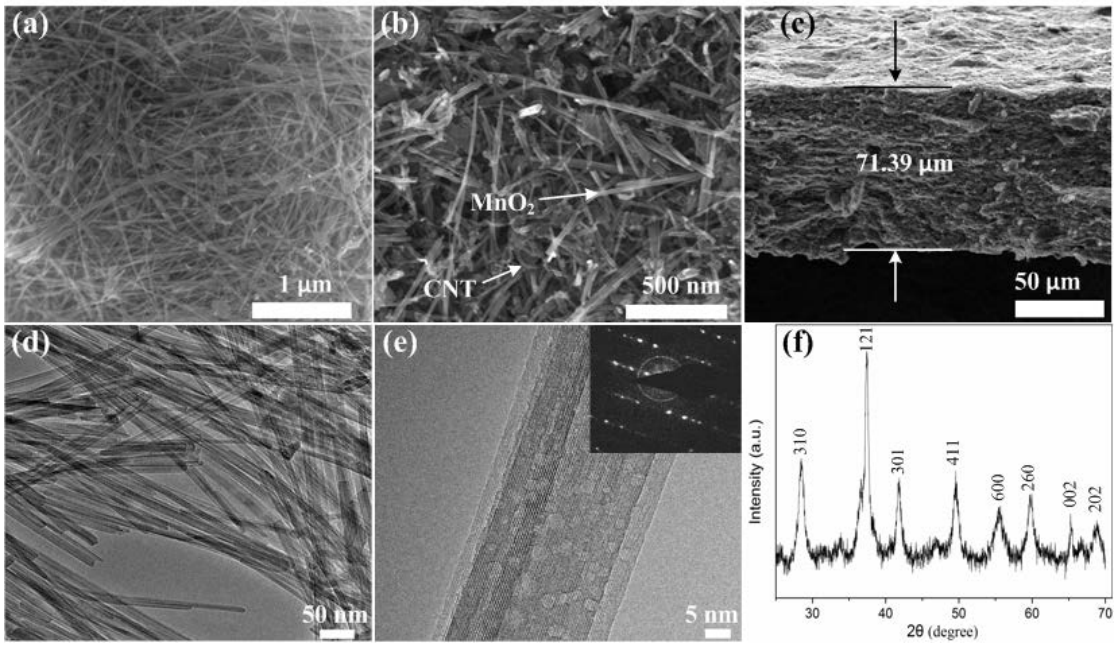

Figure 1. Characterization of MnO_2/CNTs electrodes: (a) A SEM image of MnO_2 nanowires; (b, c) The top view and the side view of MnO_2/CNTs films; (d) A TEM image of MnO_2 nanowires; (e) High resolution TEM image and the inset SAED pattern of MnO_2 nanowires showing the incomplete monocrystalline nature of MnO_2 nanowires; (f) XRD pattern of MnO_2 nanowires.

electrolyte of $LiPF_6$/EC/DMC. The morphology of MnO_2 nanowires was revealed by SEM and TEM images (Figure 1a, d). MnO_2 nanowires entangled each other with the length of several micrometers and diameters of 8 ~ 25 nm. The force of friction at the surface of MnO_2 nanowires is the major factor that maintains the structure of free-standing films. Figure 1b is a SEM image of MnO_2/CNTs composite with a mass ratio of 7:3 (This mass ratio is decided by the electrode optimization processes before fabricating SCs, and the relative data is shown in Figure S4.), revealed that there is few conglobations of CNTs, which ensures the conductive channels uniformly distributed throughout the whole film. The relationship between the mass density and the thickness of the MnO_2/CNTs film is revealed in Figure 1c. The thickness of a MnO_2/CNTs film with a total mass density of 8 mg cm^{-2} is about 71.4 μm. More

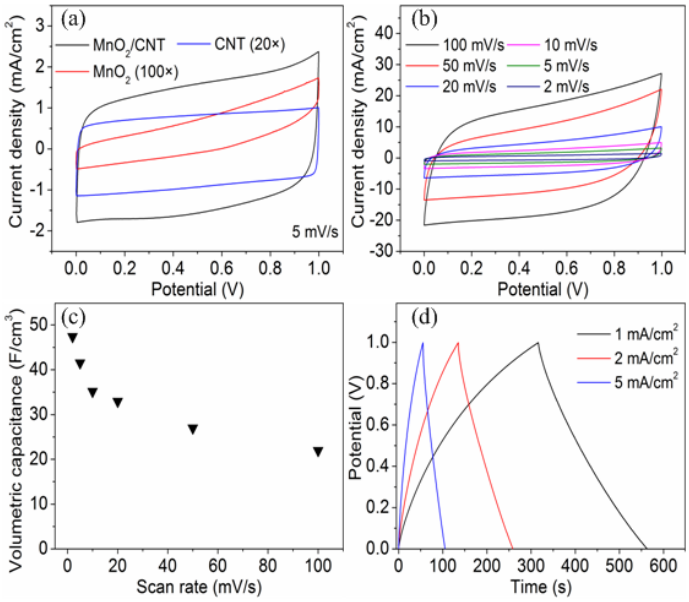

Figure 2. Electrochemical performances of the SC of MnO_2/CNTs electrodes: (a) CV curves of the SCs based on pure MnO_2 nanowires, CNTs, and MnO_2/CNTs electrodes, respectively; (b) CV curves of the MnO_2/CNTs SC at different scan rate; (c) Volumetric capacitances of the MnO_2/CNTs SC at different scan rates; (d) GCD curves of the MnO_2/CNTs SC at different current densities.

details of the structure of MnO_2 nanowires are revealed in Figure 1e. There are a certain amount of nanopores on the surface of MnO_2 nanowires. These nanopores increase the interface between nanowires and the electrolyte, which provide larger effective area for redox reaction. Furthermore, the MnO_2 nanowire has an incomplete monocrystalline structure revealed by Figure 1e and the inset selected area electron diffraction (SAED) pattern. The bright ring in the SAED pattern indicates that the nanowire contains some polycrystalline component, which may be caused by the relatively low growth temperature. The X-ray diffraction (XRD) pattern (Figure 1f) further confirmed that crystal type of the nanowire belongs to tetragonal α-MnO_2 phase (JCPDS 44-0141).[27]

Taking into account the application in practice, two free-standing MnO_2/CNTs films of the same area were sealed in a coin cell with $LiPF_6$/EC/DMC electrolyte. The electrochemical behaviour of MnO_2/CNTs films was evaluated by performing cyclic voltammetry (CV) and galvanostatic charge-discharge (GCD) characterization with two-electrode configuration. The CV curves of SCs based MnO_2 nanowires, CNTs and MnO_2 nanowires/CNTs are compared in Figure 2a. According to Y. Gogotsi and P. Simon's perspective,[28] the volumetric capacitance (or areal capacitance) of our devices are calculated because it is much closer to application. The SC fabricated by pure MnO_2 nanowires has the smallest volumetric capacitance (based on the total volume of the free-standing membranes fabricated by MnO_2 nanowires) of 107 mF cm^{-3} at a scan rate of 5 mV s^{-1}. The poor capacitance is mainly caused by the poor conductivity of MnO_2 (10^{-5}~10^{-6} S/cm, Ref.1). The electrons, produced by the redox of MnO_2, can't be transferred to the collector in time, which leads to a large amount of deactivated mass in the electrodes. In addition, high internal resistance of the pure MnO_2 electrodes results in heavy ohmic polarization, which further decreases the capacitive performance of the device. The CV curve of the SC with CNTs film electrodes presents an ideal rectangle shape that revealed the nature of electrochemical double layer capacitor. The SCs fabricated by the MnO_2/CNTs films have much higher volumetric capacitance (based on the total volume of the MnO_2/CNTs electrodes) of 41.5 F cm^{-3} at a scan rate of 5 mV s^{-1}, which is 388 times and 34 times of pure MnO_2 SCs and CNTs SCs, respectively. Compared to the previous literatures, the capacitance is substantially higher than graphene cellulose

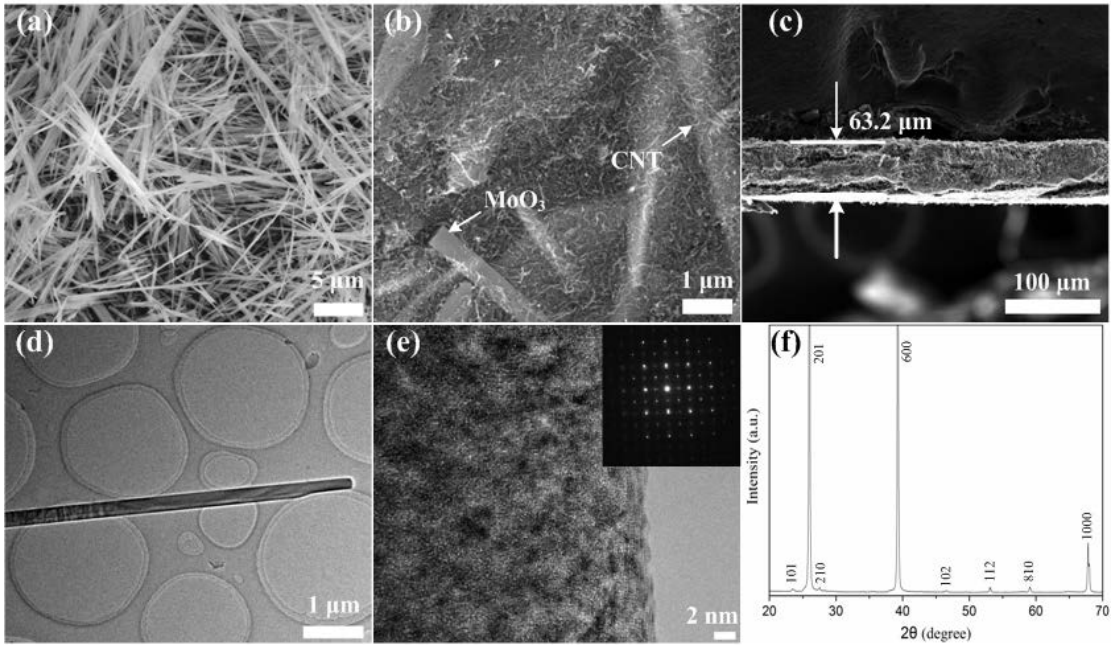

Figure 3. Characterization of MoO_3/CNTs electrodes: (a) A SEM image of MoO_3 nanobelts; (b, c) The top view and the side view of MoO_3/CNTs films; (d) A TEM image of MoO_3 nanobelts; (e) High resolution TEM image and the inset SAED pattern of MoO_3 nanobelts showing the monocrystalline nature of MoO_3 nanobelts; (f) XRD pattern of MoO_3 nanobelts.

paper based SCs,[29] TiN based SCs,[30] and some metal oxide based ASCs.[16, 23] The electrochemical performances of MnO_2/CNTs SCs have been distinctly enhanced, which attributed to the conductive network from the uniform distribution of CNTs in the electrodes. CV curves of MnO_2/CNTs SCs at different scan rates in the potential window of 0 ~ 1.0 V are showed in Figure 2b. The curves have good symmetrical shapes even at a high scan rate of 100 mV s^{-1}, indicating that the charge-discharge process in the electrodes is reversible steadily. The trend of volumetric capacitance versus different scan rates is revealed in Figure 2c. The volumetric capacitance of the MnO_2/CNTs ASC decreased from 47.4 F cm^{-3} to 22.0 F cm^{-3} as the scan rate from 2 mV s^{-1} to 100 mV s^{-1}. The rate of decay is 53.6% when the charge-discharge rate has been accelerated 50 times, which is much lower than those reported previously.[10, 16,

[30] Figure 2d shows the GCD curves of the MnO_2/CNTs SC at different current densities, in which good linear potential-time profiles are achieved, demonstrating a good capacitance performance of the device. The Coulombic efficiency of the ACS is 98.3% and 85.5% at the current density of 5 mA cm^{-2} and 1 mA cm^{-2}, respectively. The lower Coulombic efficiency at smaller current density may be caused by the accumulative effect of leakage current during the lower power process.

2.2 Characterizations of Negative Electrode Materials

Compared to abundant studies on positive electrodes materials with great progress, researches focus on negative electrode materials of transition metal oxides are sluggish due to high cost or the unsatisfactory capacitive performance.[31] Similar to the positive material of MnO_2, MoO_3 is a layer-structured material of low cost, which facilitates the injection of ions into the free spaces for exceptional electrochemical properties.[24, 32] Thus, MoO_3 nanobelts were synthesized by a simple hydrothermal method to match the positive electrode material of MnO_2. The morphology of MoO_3 nanobelts was revealed by SEM and TEM images (Figure 3a, d). The length, width and thickness of MoO_3 nanobelts are several micrometers, 90 ~ 500 nm and about 65 nm (Figure S1a, b), respectively. Figure 3b is a SEM image of MoO_3/CNTs composite with a mass ratio of 7:3, showing that MoO_3 nanobelts are encompassed by CNTs. The thickness of a MoO_3/CNTs film with a total mass density of 8 mg cm^{-2} is about 63.2 μm (Figure 3c). The rough surface of MoO_3 nanobelts showed in the high resolution TEM image (Figure 3e), is helpful to enlarge the specific surface area. A monocrystalline structure was revealed by the SAED (the inset in Figure 3e). The

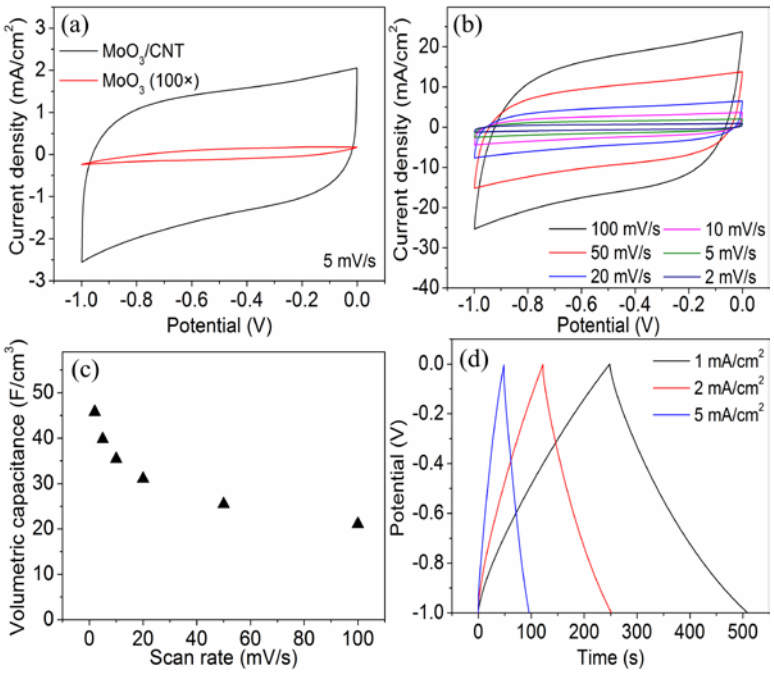

Figure 4. Electrochemical performances of the SC of MoO_3/CNTs electrodes: (a) CV curves of the SCs based on pure MoO_3 nanowires, and MoO_3/CNTs electrodes, respectively; (b) CV curves of the MoO_3/CNTs SC at different scan rate; (c) Volumetric capacitances of the MoO_3/ CNTs SC at different scan rates; (d) GCD curves of the MoO_3/CNTs SC at different current densities.

XRD pattern (Figure 3f) further confirmed that the prepared MoO_3 nanobelt has the orthorhombic structure (JCPDS 03-065-2421).[33]

The electrochemical tests of the MoO_3/CNTs free-standing films were performed in a two-electrode cell using $LiPF_6$/EC/DMC electrolyte. As illustrated in Figure 4a, MoO_3/CNTs composite exhibits better electrochemical performance than pure MoO_3 with an operation potential window of -1.0 to 0 V. SCs based MoO_3/CNTs composite with 30% CNTs have a high volumetric capacitance (based on the total volume of the MoO_3/CNTs electrodes) of 39.8 F cm^{-3} at 5 mV s^{-1}, which is much higher than the SCs based on pure MoO_3 (25 mF cm^{-3} at 5 mV s^{-1}), CNTs (1.2 F cm^{-3}), and the previous works.[15, 22, 29, 30] The dramatic improvement of the electrochemical performance of MoO_3/CNTs SCs is attributed to the better conductivity of the

composite than pure MoO_3 nanobelts(~10^{-4} S cm^{-1}).[34] The space between MoO_3 nanobelts and CNTs is favourable for ions diffusion and electrons can be transferred immediately by the conductive network of CNTs. In addition, CNTs offer better inner connectivity between MoO_3 nanobelts and furthermore participate in electrochemical double layer capacitance. Figure 4b shows CV curves at different scan rate. When the scan rate is accelerated from 2 mV s^{-1} to 100 mV s^{-1}, the symmetry of the curves just has a slight fluctuation (Figure 4a and b), implicated good rate capability of the devices. The relationship of volumetric capacitance versus scan rate is showed in Figure 4c. The volumetric capacitance of the MoO_3/CNTs ASC decreased from 45.8 F cm^{-3} to 21.1 F cm^{-3} as the scan rate from 2 mV s^{-1} to 100 mV s^{-1}. The decay rate is 54.0% when the charge-discharge rate has been accelerated 50 times, which is acceptable compared with those previous works.[10, 16, 30] Figure 4d shows the GCD curves of the MoO_3/CNTs SC at different current densities. The near triangle shapes of the GCD curves are revealed, which indicated a good capacitance performance of the device. Integrating with the previous analysis of the positive electrodes, we find that the negative electrode based on MoO_3/CNTs free-standing film matches the positive electrode from MnO_2/CNTs film well except to adjust the mass ratio of them.

2.3 Electrochemical Behaviour of ASCs and SASCs

Based on the investigation of the electrochemical performance of MnO_2/CNTs and MoO_3/CNTs composite materials, the best volumetric ratio of the anode and the cathode free-standing membranes is about 1 : 0.96 (equals mass ratio of 0.86 : 1). The more details of the middle layer used in the SASC are showed in Figure S3a and b.

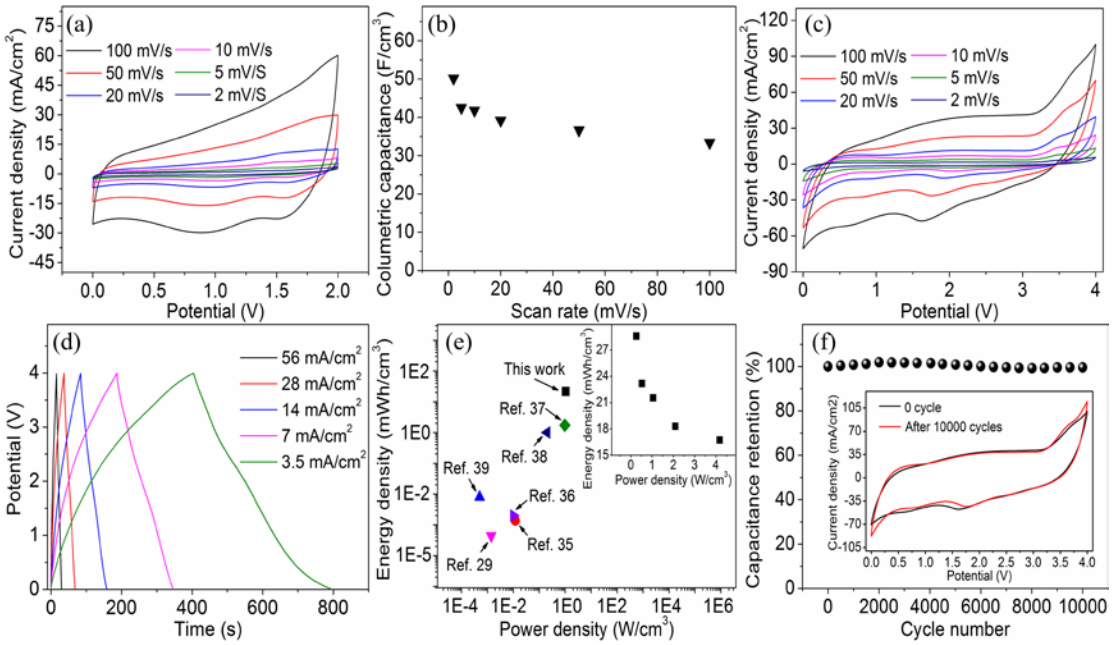

Figure 5. (a) CV curves of the ASC based on MnO_2/CNT and MoO_3/CNT composite electrodes; (b) Volumetric capacitances of the ASC at different scan rates; (c) CV curves of the SASC at different scan rates; (d) GCD curves of the SASC at different current densities; (e) Ragone plots of our SASC and some other devices; (f) Cycling performance of the optimized SASC.

Thus, optimized ASC and SASC full cells were fabricated using $LiPF_6$/EC/DMC electrolyte. Their electrochemical behaviour was evaluated by performing electrochemical measurements. Fig 5a is the CV curves of the optimized ASC at the different scan rates from 2 to 100 mV s^{-1}, and its operation potential window are as high as 0 ~ 2.0 V. The highest volumetric capacitance of the ASC is 50.2 F cm^{-3} (based on the total volume of the MnO_2/CNT and MoO_3/CNT electrodes) at a scan rate of 2 mV s^{-1}, and maintains 66.5 % of the capacitance when the scan rate has been accelerated to 100 mV s^{-1}. Benefiting from the electrochemical stability of the organic electrolyte and no hydrogen/oxygen evolution reactions, the potential window of the SASC is widened from 0 to 4.0 V. A comparison of the CV curves of ASC and SASC full cells within different potential windows is shown in Figure S5a. Figure 5c shows

CV curves of the SASC at different scan rates. The highest volumetric capacitance (based on the total volume of the anode, the cathode and the middle layer) of the full cell is 38.1 F cm^{-3} at 2 mV s^{-1}. To further investigate the performance of the SASC, we measured GCD curves at various current densities (Figure 5d). Figure 5e shows Ragone plot for energy density (*E*) and power density (*P*) of the SASC full cell, which is calculated from Figure 5d. It is notable that the highest E and P of this SASC are much higher than the previous reports.[29, 35-39] The SASC with a cell voltage of 4.0 V can exhibit an energy density of 28.6 mWh cm^{-3} at a power density of 0.26 W cm^{-3}, or 16.7 mWh cm^{-3} at 4.18 W cm^{-3}, respectively. The enhancement of energy density here is attributed to the enlarged operation potential window and the high energy density of both electrodes. The electrochemical performance is improved by combination with high energy density of metal oxide and good conductivity of CNTs.

Long cycle life is an important requirement for SCs in practice. The cycle life measurement during 10000 cycles for the SASC was carried out by repeating the CV test between 0 and 4.0 V at a scan rate of 100 mV s^{-1} (Figure 5f). The capacitance of the SASC full cell increases at the initial 3000 cycles, which is probably attributed to the improvement in the activation of the active materials and the infiltration of the electrode surface by the organic electrolyte. The capacitance retention is 99.6% when the SASC cell stands 10000 cycles, which is much better than the pseudocapacitors using aqueous electrolytes,[23, 40, 41] and some other quasi solid-state SCs with gel electrolytes (showed in Figure S7). The stable cycling performance of the device is mainly due to the well matching of the electrodes and the good stability of middle

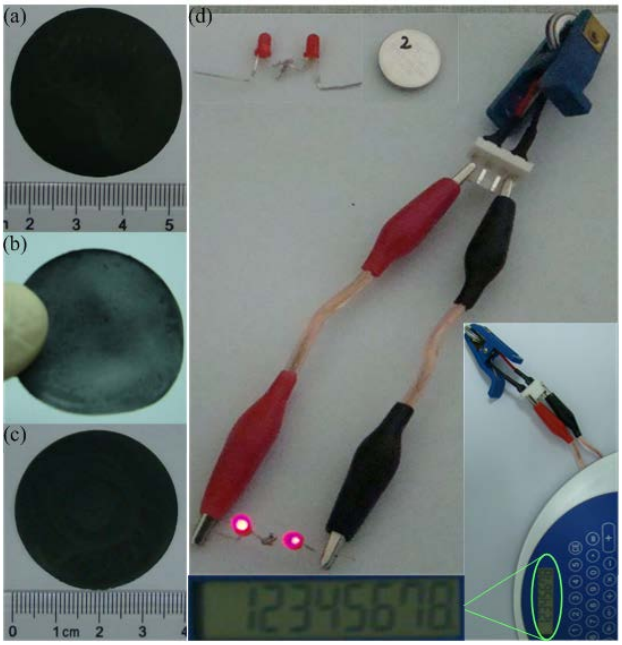

Figure 6. Photos of the free-standing films: (a) a MnO_2 nanowires/CNTs composite film; (b) the middle layer with inner-connection structure; (c) a MoO_3 nanobelts/CNTs composite film. (d) Photos of two series LEDs and a SASC full cell; two series LEDs and a calculator drove by a fully charged SASC cell; enlarged calculator display screen; respectively.

layer with inner-connection structure, further demonstrated the proper design of the SASC. The electrochemical impedance spectroscopy (EIS) analysis has been introduced when the SASC has 0 cycle and 10000 cycles, respectively (Figure S5b, and Figure S8). The Nyquist plots for 0 cycle and after 10000 cycles almost overlap, indicating perfect stability of the electrode materials in the organic electrolyte and the good reversibility of the redox, which is consistent with the results of cycle life test. In addition, the inner-connected structure used in the SASC has some more fascinating features compared the conventional approach. The relative data is shown in Figure S6. The volumetric capacitance of a SASC is about 30% higher than that of two ASCs connected in series (Figure S6a, b). The lower resistance (R_S, R_{CT}, Figure S6c) of the SASC is beneficial to the transmission of the charges and ions, which

ensures more efficient exploitation for the energy.

For application of the as-fabricated SASC, some digital photos are presented in Figure 6. The free-standing membranes of positive electrode, middle layer with inner-connection structure, and the negative electrode are exhibited in Figure 6a, 6b and 6c, respectively. Two examples for the devices of their application in practice are given, as showed in Figure 6d. When an ASC cell has been charged fully, it can easily drive a calculator (the nominal voltage is 1.5 V). As for a SASC cell, two series LEDs (the nominal voltage of each one is 1.8 V) are lightened after full charging. The high output voltage character of the SASC provides more convenience to meet the high voltage demands than that of conventional series SCs (three series SCs to power one LED).[29, 42]

3 Conclusion

In summary, we have successfully developed an SASC based on free-standing membranes. MnO_2/CNTs and MoO_3/CNTs composite films are obtained for the positive and negative electrode, respectively. We demonstrated that coupling the MnO_2/CNTs and MoO_3/CNTs composite can produce ASCs with high energy and high output voltage. The design of SASC by inserting a middle layer with inner-connection structure between the positive and negative electrode is adopted, which provides a large operation voltage window of the device. The SASC shows high volumetric capacitance, high energy density, and good long-term stability at a potential window of 4.0 V in $LiPF_6$/EC/DMC electrolyte. The SASC with hybridized structure presented here aims at simplifying the fabricating process, lowering the cost

and using environmental friendly materials for applications in practice. The simple fabricating process and the cell configuration of the SASC provide a promising research direction for the next generation, low-cost SCs with high energy density and high output voltage demands.

Acknowledgements

This work was supported by the National Basic Research Program (Grant 2011CB933300) of China, the National Natural Science Foundation of China (Grants 11204093 and 11074082), and the Fundamental Research Funds for the Central Universities (HUST: Grants 2014TS124 and 2013TS033).

Notes and references

1. W. Chen, R. B. Rakhi, L. B. Hu, X. Xie, Y. Cui and H. N. Alshareef, *Nano Lett.*, 2011, **11**, 5165-5172.
2. A. S. Arico, P. Bruce, B. Scrosati, J. M. Tarascon and W. Van Schalkwijk, *Nat. Mater.*, 2005, **4**, 366-377.
3. P. Simon and Y. Gogotsi, *Nat. Mater.*, 2008, **7**, 845-854.
4. L. L. Zhang and X. S. Zhao, *Chem. Soc. Rev.*, 2009, **38**, 2520-2531.
5. J. R. Miller and P. Simon, *Science*, 2008, **321**, 651-652.
6. H. K. Jeong, M. Jin, E. J. Ra, K. Y. Sheem, G. H. Han, S. Arepalli and Y. H. Lee, *Acs Nano*, 2010, **4**, 1162-1166.
7. A. Balducci, R. Dugas, P. L. Taberna, P. Simon, D. Plee, M. Mastragostino and S. Passerini, *J. Power Sources*, 2007, **165**, 922-927.
8. C. Zhou, Y. W. Zhang, Y. Y. Li and J. P. Liu, *Nano Lett.*, 2013, **13**, 2078-2085.
9. Y. W. Cheng, H. B. Zhang, S. T. Lu, C. V. Varanasiad and J. Liu, *Nanoscale*, 2013, **5**, 1067-1073.
10. C. Y. Foo, A. Sumboja, D. J. H. Tan, J. Wang and P. S. Lee, *Adv. Energy Mater.*, 2014, *DOI: 10.1002/aenm.201400236.*
11. Fan Zhang, Yanhong Lu, Xi Yang, Long Zhang,Tengfei Zhang, Kai Leng, Yingpeng Wu, Yi huang, Yanfeng Ma and Yongsheng Chen. *Small.* 2014, **10**, 2285-2292.
12. M. Sawangphruk, M. Suksomboon, K. Kongsupornsak,J. Khuntilo, P. Srimuk, Y. Sanguansak, P. Klunbud, P. Suktha and P. Chiochan. *J. Mater. Chem. A.*, 2013, **1**, 9630-9636.
13. Y. G. Wang and Y. Y. Xia, *Electrochem. Commun.*, 2005, **7**, 1138-1142.
14. Z. J. Fan, J. Yan, T. Wei, L. J. Zhi, G. Q. Ning, T. Y. Li and F. Wei, *Adv. Funct. Mater.*, 2011, **21**, 2366-2375.
15. J. Yan, Z. J. Fan, W. Sun, G. Q. Ning, T. Wei, Q. Zhang, R. F. Zhang, L. J. Zhi and F. Wei, *Adv. Funct. Mater.*, 2012, **22**, 2632-2641.
16. J. Y. Tao, N. S. Liu, L. Y. Li and Y. H. Gao, *Nanoscale*, 2014, **6**, 2922-2928.
17. H. L. Wang, Y. Y. Liang, T. Mirfakhrai, Z. Chen, H. S. Casalongue and H. J. Dai, *Nano Res.*, 2011, **4**,

729-736.

18. H. Jiang, J. Ma and C. Z. Li, *Adv. Mater.*, 2012, **24**, 4197-4202.
19. X. H. Lu, T. Zhai, X. H. Zhang, Y. Q. Shen, L. Y. Yuan, B. Hu, L. Gong, J. Chen, Y. H. Gao, J. Zhou, Y. X. Tong and Z. L. Wang, *Adv. Mater.*, 2012, **24**, 938-944.
20. M. F. L. De Volder, S. H. Tawfick, R. H. Baughman and A. J. Hart, *Science*, 2013, **339**, 535-539.
21. E. Frackowiak and F. Beguin, *Carbon*, 2001, **39**, 937-950.
22. Y. Jin, H. Y. Chen, M. H. Chen, N. Liu and Q. W. Li, *Acs Appl. Mater. Inter.*, 2013, **5**, 3408-3416.
23. J. Xu, Q. F. Wang, X. W. Wang, Q. Y. Xiang, B. Hang, D. Chen and G. Z. Shen, *Acs Nano*, 2013, **7**, 5453-5462.
24. J. Chang, M. Jin, F. Yao, T. H. Kim, V. T. Le, H. Yue, F. Gunes, B. Li, A. Ghosh, S. Xie and Y. H. Lee, *Adv. Funct. Mater.*, 2013, **23**, 5074-5083.
25. M. Simoes, Y. Mettan, S. Pokrant and A. Weidenkaff, *J. Phys. Chem. C*, 2014, **118**, 14169-14176.
26. C. K. Huang, J. S. Sakamoto, J. Wolfenstine and S. Surampudi, *J. Electrochem. Soc.*, 2000, **147**, 2893-2896.
27. X. Wang and Y. D. Li, *J. Am. Chem. Soc.*, 2002, **124**, 2880-2881.
28. Y. Gogotsi and P. Simon, *Science*, 2011, **334**, 917-918.
29. Z. Weng, Y. Su, D. W. Wang, F. Li, J. H. Du and H. M. Cheng, *Adv. Energy Mater.*, 2011, **1**, 917-922.
30. X. H. Lu, G. M. Wang, T. Zhai, M. H. Yu, S. L. Xie, Y. C. Ling, C. L. Liang, Y. X. Tong and Y. Li, *Nano Lett.*, 2012, **12**, 5376-5381.
31. Q. T. Qu, S. B. Yang and X. L. Feng, *Adv. Mater.*, 2011, **23**, 5574-5580.
32. T. Brezesinski, J. Wang, S. H. Tolbert and B. Dunn, *Nat. Mater.*, 2010, **9**, 146-151.
33. R. L. Liang, H. Q. Cao and D. Qian, *Chem. Commun.*, 2011, **47**, 10305-10307.
34. L. Q. Mai, B. Hu, W. Chen, Y. Y. Qi, C. S. Lao, R. S. Yang, Y. Dai and Z. L. Wang, *Adv. Mater.*, 2007, **19**, 3712-3716.
35. B. Duong, Z. Yu, P. Gangopadhyay, S. Seraphin, N. Peyghambarian and J. Thomas, *Adv. Mater. Interfaces*, 2014, **1**, DOI: 10.1002/admi.201300014.
36. P. H. Yang, X. Xiao, Y. Z. Li, Y. Ding, P. F. Qiang, X. H. Tan, W. J. Mai, Z. Y. Lin, W. Z. Wu, T. Q. Li, H. Y. Jin, P. Y. Liu, J. Zhou, C. P. Wong and Z. L. Wang, *Acs Nano*, 2013, **7**, 2617-2626.
37. J. Ren, L. Li, C. Chen, X. Chen, Z. Cai, L. Qiu, Y. Wang, X. Zhu and H. Peng, *Adv. Mater.*, 2013, **25**, 1155-1159, 1224.
38. J. Ren, W. Y. Bai, G. Z. Guan, Y. Zhang and H. S. Peng, *Adv. Mater.*, 2013, **25**, 5965-5970.
39. T. Chen, L. B. Qiu, Z. B. Yang, Z. B. Cai, J. Ren, H. P. Li, H. J. Lin, X. M. Sun and H. S. Peng, *Angew. Chem. Int. Edit.*, 2012, **51**, 11977-11980.
40. L. B. Hu, W. Chen, X. Xie, N. A. Liu, Y. Yang, H. Wu, Y. Yao, M. Pasta, H. N. Alshareef and Y. Cui, *Acs Nano*, 2011, **5**, 8904-8913.
41. S. W. Lee, J. Kim, S. Chen, P. T. Hammond and Y. Shao-Horn, *Acs Nano*, 2010, **4**, 3889-3896.
42. S. H. Li, D. K. Huang, B. Y. Zhang, X. B. Xu, M. K. Wang, G. Yang and Y. Shen, *Adv. Energy Mater.*, 2014, DOI: 10.1002/aenm.201301655.